An Aquatic Robot Propelled by an Internal Rotor

Beau Pollard and Phanindra Tallapragada

Abstract—Unmanned aquatic vehicles and robots are of tremendous importance in a variety of applications. In this paper, we present the model of an underactuated aquatic robot that is propelled by an internal rotor. The propulsion of the robot is based on the exchange of momentum between the body and water that is mediated by the creation of vorticity at the trailing edge of the robot. The robot does not have any external fins, propellers, or articulated joints allowing for very easy fabrication. Experimental data on its locomotion and maneuverability are presented.

Index Terms—Aquatic robots, mobile robots, swimming robots.

I. Introduction

UNMANNED aquatic vehicles and robots are of great interest in applications ranging from exploration, environmental monitoring, inspection of underwater structures, search and rescue operations, surveillance, and numerous military applications. The development of unmanned underwater robots has, on one hand, been inspired by natural swimmers. Scientists and engineers have turned to studying natural swimmers such as fish, crustaceans, marine mammals such as whales, cephalopods such as squid, and other invertebrates such as jelly fish. These studies have led to the development of many bio-inspired aquatic robots, perhaps the most famous of which is MIT's robot-tuna, [1], [2]. In particular, the locomotion of carangiform and subcarangiform fish has inspired the design of robots with a compliant body or a compliant tail, see for example, [3]–[9], as well as articulated joints to imitate fish vertebrae, [10], [11] or the caudal fin, [12]. The propulsive power of the fin-like appendages is demonstrated by robots that are inspired by animals other than fish too, such as the turtle inspired U-Cat robot [13].

Another class of aquatic robots is that of underwater gliders which rely on buoyancy driven propulsion. Some examples include the "Seaglider," "Slocum," and "Spray," [14]–[17]. More recently, miniature versions of underwater gliders weighing as little as 4 kg have been developed [18].

In this paper, we present a novel fish-like swimming robot that propels itself through the motion of an internal rotor. The mechanism of propulsion as well as steering in a horizontal plane is the internal rotor. This form of propulsion is motivated by the interpretation of vortex shedding past the trailing edge of a hydrofoil as a nonholonomic constraint [19]. Nonholonomic constraints allow the motion of a body with fewer shape variables (degrees of actuation) than would be required otherwise. A parallel inspiration for the robot is the mechanics of swimming of carangiform fish, with the shape variable being the motion of the internal rotor. In a series of papers, [19]–[22], one of the authors and other collaborators demonstrated these theoretical concepts through the use of simplified models of locomotion in an ideal fluid with singular distributions of vorticity.

This paper presents a proof-of-concept robot that utilizes these principles and demonstrates its propulsive and maneuvering capabilities. This being the primary goal, we restrict this paper to demonstrating the motion of a neutrally buoyant planar swimmer. The paper discusses a design of the robot, its inertia characteristics, and its propulsion mechanism and presents results on its locomotion. Several different cases of actuation are discussed and the results on the speed of the robot in these cases are presented. We also discuss one technique on how the underactuated robot could maneuver by changing its heading angle.

The principal contribution of the paper is the demonstration of a workable prototype that utilizes the principles of fish-like swimming described in [19]–[22]. The robot does not have any articulated joints, propellers, or a deformable body that relies on smart materials. It is therefore easy to fabricate and can have potential stealth properties. The simple means of actuation that is proposed will allow the investigation of several novel control strategies that rely on nonholonomic constraints and the fluid–body interaction. On a more fundamental note, the robot can also be a testbed to understand the interaction of a body with vorticity and the process of extracting propulsive energy from the fluid. The robot can also inspire the design of hybrid underwater gliders that rely on both internal rotors and buoyancy for both propulsion and navigation.

The paper is organized as follows: in Section II, we first briefly review the idealized model of a swimmer with an internal rotor and its relation to fish-like swimming. The goal of this review is to motivate the design of the physical model rather than an exact quantitative comparison with the theoretical model. The review is qualitative and omits several details which can be found in other papers such as [19]–[22] and [23]–[26]. We then discuss the design of the planar swimming robot in Section III and, in Section IV, discuss the performance of this robot.

II. REVIEW OF SWIMMING AT HIGH REYNOLDS NUMBER

The Reynolds number determines the importance of various forces that propel or hinder a swimming body. In the case of even small aquatic animals that move slowly, for example, those with a length, $d = 0.1$ m, and a steady swimming speed, $v = 0.1$ m/s, the Reynolds number is $Re = \frac{vd}{\nu} = 10^4$, where ν the kinematic of viscosity of water is approximately 10^{-6} m^{2}s^{-1}. At even such moderate Reynolds numbers, the magnitude of viscous forces is small compared to the inertial forces. For bodies that are larger and or swim faster, the Reynolds number can be on the order of 10^6. Thus, assuming the fluid to an ideal fluid is a very good first approximation.

When a solid body moves through a fluid at a steady velocity, the fluid around the body is displaced. Thus, the motion of the solid body imparts a certain amount of momentum (or more precisely the Kelvin impulse) to the fluid. This momentum that is imparted to the fluid depends on the orientation of the body. For example, a slender rod moving in the axial direction imparts a much smaller momentum to the fluid than a slender rod moving in a direction transverse to the axis. It can be shown [27] that the momentum imparted to the fluid is equivalent to the solid body having an additional mass, the so-called added mass, that is dependent on the orientation of the body.

The added inertia of a body is an important factor in undulatory aquatic locomotion. As a body changes shape in a periodic fashion, the added inertia changes periodically. Conservation of momentum of the body and fluid ensures that the body moves as it changes shape. However, the conservation of momentum also ensures that net locomotion does not occur if there exists only one shape variable [28], [29]. A body with only one shape varying parameter can achieve net locomotion if additional constraints are placed on its motion. In fact such a constraint is naturally caused by the creation of vorticity.

If a body has a sharp tip (such as the trailing edge of a fin), fluid comes off the body tangentially rolling in vortices. Physically, it is the viscosity of the fluid that causes the creation of vorticity at a sharp tip. Thus, while one can ignore viscous forces while analyzing the motion of a body at a high Reynolds number, a mechanism of vortex shedding at a sharp tip has to be incorporated. In the case of inviscid fluid approximation, this is traditionally done via the Kutta–Joukowski condition. The Kutta–Joukowski condition specifies the vorticity creation at the trailing edge of a sharp tip to ensure that the fluid comes off tangentially. The creation of vorticity changes the velocity field of the fluid and pressure distribution on the surface of the body. This can also be interpreted in terms of the conservation of momentum; the addition of vorticity changes the momentum of the fluid and the momentum of the body changes in a manner that conserves the total momentum of the body and the fluid system. We take the second approach to calculate the influence of the vorticity on the motion of the body.

A. Mathematical Model of a Swimming Joukowski Foil in an Ideal Fluid

Consider a Joukowski foil surrounded by fluid of unit density that extends to infinity in a two-dimensional plane, represented
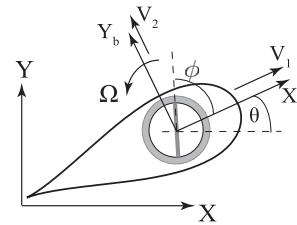

Fig. 1. Spatially fixed frame of reference is described by the X- and Y-axes, while the body axes X_b and Y_b are collocated with and oriented instantaneously along the body. The velocity of the foil is (V_1, V_2) in the body axes.

by the complex domain $\mathbb{C}$. The geometry and motion of the foil are described by mapping its boundary from a circle $\mathcal{C}$ of radius r_c centered at the origin in the mapped plane through the Joukowski transformation

$$z = F(\zeta) = \zeta + \zeta_c + \frac{a^2}{\zeta + \zeta_c} \qquad (1)$$

where $\zeta_c \in \mathbb{C}$ and $a \in \mathbb{R}$. We refer to the plane of the foil's motion as the foil plane (z-plane) and the plane of the circle's motion as the circle plane (ζ-plane). For the shape of the foil shown in Fig. 1, $\zeta_c \in \mathbb{R}$. The preimage of the sharp trailing edge of the foil is given by $\zeta_t = a - \zeta_c$. The transformation is conformal everywhere in the open set $|\zeta_c| > r_c$. The derivative of the transformation

$$F'(\zeta) = 1 - \frac{a^2}{(\zeta + \zeta_c)^2}$$

exists everywhere except at ζ_t.

Two frames of reference can be used to describe the motion of the foil. The first is a spatially fixed frame of reference denoted by the X- and Y-axes in Fig. 1. The second frame of reference, denoted by X_b and Y_b, is collocated with the body and aligned with a chosen axes of the body. Motion in one frame can be transformed to the other through the use of a rotation operator, $\mathbf{R}$. The foil has three degrees of freedom; it can translate with velocity $\mathbf{V} = (V_1, V_2)$ and rotate about its center with angular velocity $\Omega = \dot{\theta}$, as shown in Fig. 1. The velocity of the foil in the spatially fixed frame is denoted by $\mathbf{U} = (U_1, U_2)$, and can be obtained from the velocity of the foil in the body frame through the transformation, $\mathbf{U} = \mathbf{RV}$. The foil contains a heavy balanced rotor that is not in contact with the fluid. The rotor's moment of inertia is denoted by I_r, the relative angle it makes with the longitudinal axis, X_b, is denoted by ϕ, and the relative angular velocity is denoted by $\omega = \dot{\phi}$.

The configuration space of the swimmer moving in an ideal fluid is thus $\mathbf{Q} = \mathbf{SE2} \times \mathbf{S}$ with local coordinates (x, y, θ, ϕ) where (x, y) and θ are the position and orientation of the foil with respect to a spatially fixed frame of reference.

The fluid is assumed to be ideal almost everywhere, with a singular distribution of vorticity modeled by N point vortices with circulations Γ_n located at points ζ_n in the circle plane. Therefore, the motion of the fluid is governed by a linear superposition of potential functions. Following [27] and [30], the complex potential, $W(z = F(\zeta)) = w(\zeta)$, describing the velocity of the fluid in a frame of reference collocated with the foil may be decomposed in terms of its dependence on the transla-

tion of the foil, the rotation of the foil and each of the N point vortices in the form

$$w(\zeta) = W(z) = V_1 w_1(\zeta) + V_2 w_2(\zeta) + \Omega w_3(\zeta)$$

$$+ \sum_{n=1}^{N} w_v^n(\zeta). \tag{2}$$

Here w_1, w_2, and w_3 are the rigid-body potential functions (the so-called Kirchhoff potential functions), due to the translation of the foil in the X_b- and Y_b-directions and rotation about the Z-axis, respectively, and w_v^n is the potential due to the nth point vortex and its image point vortex located inside the foil according to the *Milne–Thomson Circle Theorem* [30]. On the boundary of the solid body, the real components $\phi_v^n(\zeta)$, $\phi_1(\zeta)$, $\phi_2(\zeta)$, $\phi_3(\zeta)$ of the complex potentials $w_v^n(\zeta)$, $w_1(\zeta)$, $w_2(\zeta)$, $w_3(\zeta)$ satisfy the boundary condition that the fluid has no relative normal velocity. The Kirchhoff potentials and the vortex potential can be obtained from these boundary condition, [27], and these functions for the Joukowski foil are well known

$$w_1(\zeta) = \frac{-r_c^2}{\zeta} + \frac{a^2}{(\zeta + \zeta_c)},$$

$$w_2(\zeta) = -\imath \left(\frac{r_c^2}{\zeta} + \frac{a^2}{(\zeta + \zeta_c)} \right),$$

$$w_3(\zeta) = -\imath \left(\frac{r_c^2}{\zeta} \left(\zeta_c + \frac{a^2}{\zeta_c} \right) - \left(\frac{a^2 \zeta_c}{r_c^2 - |\zeta_c|^2} + \frac{a^2}{\zeta_c} \right) \frac{a^2}{\zeta + \zeta_c} \right)$$

$$w_v^n(\zeta) = \frac{\Gamma}{2\pi\imath} \left(\log(\zeta - \zeta_n) - \log\left(\zeta - \frac{r_c^2}{\overline{\zeta_n}} \right) \right)$$

see, for example, [25], [26], and [22] for further details.

B. Coupled Motion of the Foil and Fluid

The conservation of the linear and angular momentum of the fluid–body interacting system is given by the equation:

$$\mathbf{I} \begin{pmatrix} V_x \\ V_y \\ \Omega \end{pmatrix} + \begin{pmatrix} \mathbf{L_v} \\ \mathbf{A_v} \end{pmatrix} =, \begin{pmatrix} \mathbf{R}^T \mathbf{L}_0 \\ \mathbf{A}_0 + I_r \ddot{\phi} \end{pmatrix} \tag{3}$$

where $\mathbf{I}$ is the effective (3×3) inertia tensor of the body (expressed in body coordinates) that includes the added mass due to the momentum imparted to the fluid caused by the motion of the body. The initial linear impulse of the system is denoted by $\mathbf{L}_0$ and consists of two components, L_{0x} and L_{0y}, in the X- and Y-directions, respectively. The angular impulse of the body–fluid system is denoted by $\mathbf{A}_0$ which is in a direction perpendicular to the plane of motion. If the body starts from rest in a fluid that is also initially at rest, both $\mathbf{L}_0$ and $\mathbf{A}_0$ are zero. The total angular impulse of the system changes exactly at the rate at which angular momentum of the internal rotor changes, i.e., $I_r \ddot{\phi}$. The linear and angular impulse of the fluid due to the discrete point vortices depends only on the relative position of the vortices with respect to the body and can be simplified to obtain analytical expressions, $\mathbf{L}_v(\zeta_n, \Gamma_n)$ and $\mathbf{A}_v(\zeta_n, \Gamma_n)$, for details see [21], [24]–[26]. Here too, the linear impulse of the fluid due to the vortices consists of two components, L_{vx} and L_{vy} in the X- and Y-directions, respectively.

The vortices themselves are advected by the fluid with a velocity that is obtained from the potential function defined at the location of each of the vortices, respectively. This potential function evaluated at the location of the kth vortex is given by

$$W_{sv}^k = W(z) - \frac{\Gamma}{2\pi\imath} \log(z - z_k) \tag{4}$$

which is the same as given in (2) except that the self-induced velocity of a point vortex is zero. The velocity of the kth vortex is

$$\dot{\zeta}_k = \left(\overline{\frac{dW_{sv}^k}{dz}} - (U_1 + \imath U_2 + \imath \Omega z_k) \right) \frac{1}{F'(\zeta)}. \tag{5}$$

The position of the kth vortex in the circle plane is calculated and its corresponding location in the fluid is obtained via the Joukowski transformation.

Equations (3) and (5) together provide a description of the coupled interaction between the foil-shaped body and the fluid. While (3) is a set of three algebraic equations, (5) is a set of $2N$ ordinary differential equations where N is the number of vortices in the fluid. If N is large (in the thousands), the computational time of the simulation increases significantly. A reduced-order model for the motion of the foil with unsteady point vortices is possible, see, for example, [21], that reduces the computational time by orders of magnitude. However, in the current paper, we choose not to discuss the mathematical details of the reduction and instead provide a description of only the basic body–vortex (fluid) interaction model that is sufficient to motivate the development of the physical robot.

C. Creation of New Vorticity

The idealized boundary conditions allow the fluid to slip along the surface of the foil, but at the trailing edge of the foil, which is a singularity of the Joukowski transformation, the derivative $F'(\zeta)$ vanishes, causing the velocity of the fluid in the circle plane to become undefined. The only physically allowable value for the fluid velocity at the trailing edge in the foil plane is zero; this is the Kutta condition. The Kutta condition requires that at the preimage ζ_t of the trailing edge

$$\frac{dw(\zeta)}{d\zeta} \bigg|_{\zeta = \zeta_t} = 0. \tag{6}$$

The Kutta condition represents an affine nonholonomic constraint on the velocity of the foil [19]. In a simplified numerical simulation, this condition can be enforced at (frequent) regular intervals through the shedding of new vortices. At every instant, a new vortex is added at the trailing edge, the momentum of the foil has to be adjusted in a manner that keeps the total linear and angular momentum of the system constant. This can be done by adjusting the velocity and angular velocity of the foil at the instant a vortex is created. The circulation of the newly added vortex, Γ_{N+1}, can be fixed in such a way that the total linear and angular impulse are simultaneously conserved, as

$$\mathbf{I} \begin{pmatrix} \Delta V_x \\ \Delta V_y \\ \Delta \Omega \end{pmatrix} + \Gamma_{N+1} \begin{pmatrix} \Delta \mathbf{L}_v \\ \Delta \mathbf{A}_v \end{pmatrix} = 0 \tag{7}$$
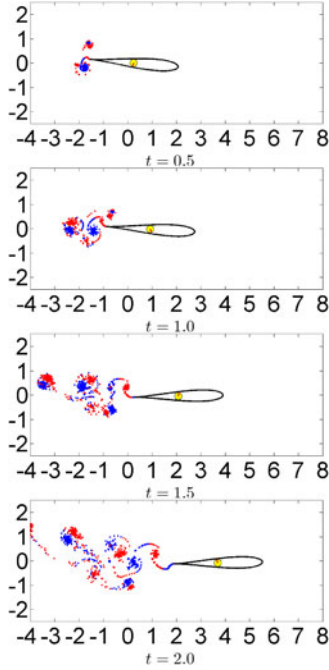
Fig. 2. Snapshots of the simulation of the motion of foil with an internal rotor that executes periodic rotations. The red dots denote vorticity with a clockwise circulation while blue dots denote vorticity with a counter clockwise circulation. The yellow circle interior to the foil represents the internal rotor. The number of point vortices in the figure shown in the last panel is 2000.

where $(\Delta V_x, \Delta V_y, \Delta \Omega)$ are impulsive changes in the velocity of the foil and $(\Delta \mathbf{L}_v, \Delta \mathbf{A}_v)$ are changes in the fluid impulse corresponding to the addition of a vortex of unit circulation. When the time intervals between the addition of two consecutive vortices are small, the changes in the velocity of the foil occur in small increments. Physically the viscosity of the fluid forces it to come off tangentially at the trailing edge and roll up into vortices. It follows that whenever a new vortex is added to the fluid, the foil receives an impulsive kick.

D. Simulation

To demonstrate the interaction of the foil with the fluid and the effect of vortex creation, the locomotion of the foil is simulated for the case where the internal rotor executes periodic oscillations. In particular, the panels in Fig. 2 show the position of the foil and the evolution of the vortex wake behind its trailing edge for the case where the relative angle of the internal rotor varies as $\phi = \frac{\pi}{6} \sin 10t$.

E. Bioinspiration From Fish-Like Swimming

The fish-like periodic deformations of the hydrofoil can be obtained by periodically varying the parameter a in the Joukowski transformation (1). Such deformations introduce an additional potential function, $w_s(\zeta)$, since the boundary conditions for the fluid change with the physical shape of the body. The total po-
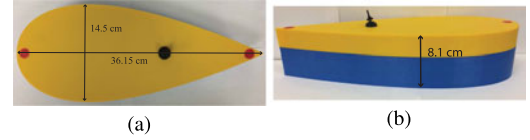

Fig. 3. (a) Geometry of the robot's body modeled on a NACA 0030 airfoil and (b) the body is made of two pieces which can be screwed on to each other.
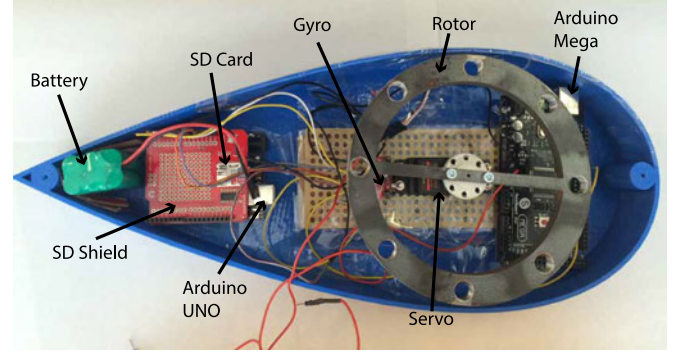

Fig. 4. Configuration of all components inside the robot's body.

tential function is still obtained via super position

$$w(\zeta) = V_1 w_1(\zeta) + V_2 w_2(\zeta) + \Omega w_3(\zeta)$$

$$+ \sum_{n=1}^{N} w_v^n(\zeta) + w_s(\zeta). \tag{8}$$

$$\mathbf{I} \begin{pmatrix} V_x \\ V_y \\ \Omega \end{pmatrix} + \begin{pmatrix} \mathbf{L_v} \\ \mathbf{A_v} \end{pmatrix} = \begin{pmatrix} \mathbf{R}^T \mathbf{L_0} - \mathbf{L_s} \\ \mathbf{A} - \mathbf{A_s} \end{pmatrix}. \tag{9}$$

Equations (9) and (3) have a similar form with the difference occurring in the right-hand side. For a foil driven by a rotor, the motion of the rotor directly affects the angular impulse which is coupled to the linear motion of the body. The relative orientation of the rotor represents an abstract shape variable. In the case of a deformable fish-like body, the shape variable is the physical shape itself and periodic changes in the shape imparts momentum to the foil. In both cases there is one actuation variable. In the case of rigid foil, this actuation variable is ϕ while in the case of the deformable foil this is the parameter a. A detailed discussion of the motion of a deformable foil can be found in [26], [25], and [22].

III. DESIGN OF AN AQUATIC ROBOT PROPELLED BY AN INTERNAL ROTOR

The horizontal cross section of the aquatic robot is modeled to have the geometry of a NACA 0030 airfoil which has a length of 35 cm and is 14 cm at its widest with no camber, see Fig. 3. This cross section is extruded to form a shell with a height of 8.1 cm, with the thickness of the walls being 0.25 cm. The body of the robot is made of ABS plastic.

The arrangement of components inside the robot is shown in Fig. 4. The balanced rotor consists of a steel ring of outer diam-

eter 13.2 cm and an inner diameter of 10.2 cm with a thickness of 0.95 cm. The moment of inertia of the rotor through an axis passing through its center is 14.661 kg·cm^2. The rotor is driven by a S9352HV Futaba servo motor which is bolted to the bottom of the robot's body. The servo is controlled using a SainSmart MEGA 2560 controller. A SparkFun Triple Axis Accelerometer and Gyro Breakout-MPU-6050 is positioned directly behind the servo, in the approximate center of gravity of the robot, to measure the angular velocity of the robot. The gyro data received by the accelerometer are saved onto a SanDisk ultra 32 GB microSD card, using a SparkFun microSD shield connected to an Arduino UNO. The Arduino UNO is also used to control the accelerometer. The robot is powered by a Ni-MH 900 mAh 7.2 V battery pack. The only component that protrudes out of the robot's body is a plastic two position toggle switch, which is used to turn the power supplied to the components ON and OFF. The total weight of the robot with all the components is 1.095 kg.

IV. EXPERIMENTS ON THE MOTION OF THE ROBOT

Several experiments were performed to test the feasibility of the planar motion of the robot. These tests were performed in a pool that was 2.4-m long and 1.2-m wide with the height of the water in it being 32 cm. A grid with horizontal and vertical lines spaced every 10 cm was placed on the bottom of the pool. A video camera placed over the center of the pool at a height of 2.15 m was used to record the motion of the robot across the length of the pool. The recorded images show the robot's location on a grid allowing one to measure its average velocity and displacement. All the experiments involved the motion of the robot in a horizontal plane, i.e., the depth of the robot is constant.

A. Straight-Line Motion

The robot's motion is never purely along a straight line, since any motion of the rotor changes the heading angle of the robot. However, the robot can execute straight-line motion on the average, as will be demonstrated, if the motion of the internal rotor is periodic. Since the rotor is driven by a servo, a natural periodic motion of the rotor is such that its angular velocity is piecewise constant

$$\omega(t) = \begin{cases} \omega_r & : nT < t \le nT + \frac{T}{2} \\ -\omega_r & : nT + \frac{T}{2} < t \le (n+1)T \end{cases} \quad (10)$$

where n is a non-negative integer and

$$T = \frac{4\phi_r}{\omega_r}.$$

In (10), ω_r is the magnitude of the angular velocity of the rotor and ϕ_r represents the amplitude of the oscillations of the rotor. These two parameters can be varied independently to change the characteristics of the motion of the robot. In our experiments, we have considered nine possible combinations of these parameters
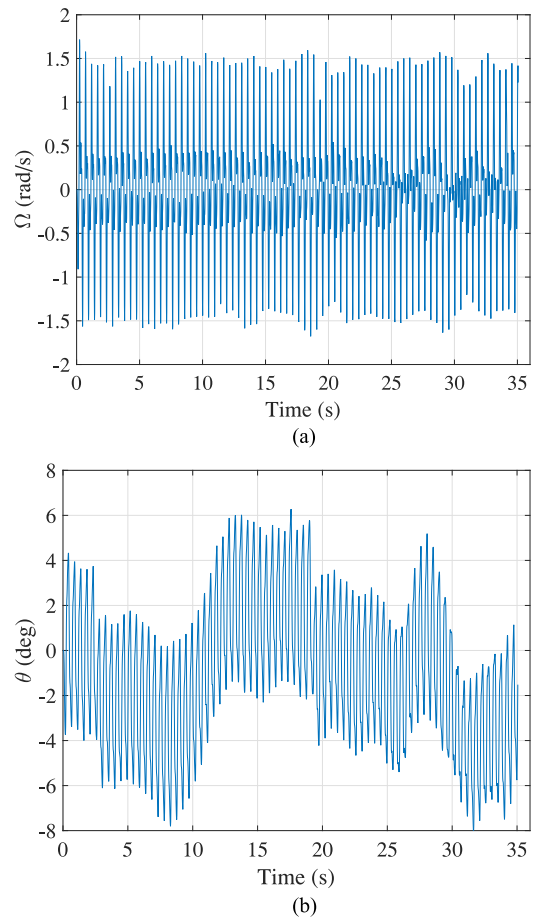

Fig. 5. Average straight-line motion: (a) Angular velocity and (b) heading angle of the robot for the case where $\phi_r = \pi/3$ and $\omega_r = 2.09\pi$.

with the following different values of the parameters with

$$(\omega_r, \phi_r) \in \{2.98\pi, 2.09\pi, 1.76\pi\} \times \left\{\frac{4\pi}{9}, \frac{\pi}{3}, \frac{\pi}{4}\right\}. \quad (11)$$

The largest values of ω_r and ϕ_r were chosen based on the limitations of the particular servo being used. Smaller values of ω_r lead to the robot attaining very small velocities.

At the start of the experiments, the robot was placed in the pool with its body axes parallel to the inertial axes of the pool. The rotations of the internal rotor cause the robot to have a varying heading angle, $\theta(t)$ while propelling itself forward. The angular velocity of the robot is measured by the gyro and stored on the SD card. After the experiment, this data are numerically integrated using the trapezoidal rule to obtain the heading angle, $\theta(t)$. Fig. 5(a) and (b) shows the angular velocity of the robot and its heading angle, respectively, for the case where the inputs are $\omega_r = 2.98\pi$ and $\phi_r = \pi/3$.

It can be observed in Fig. 5(b) that both the angular velocity and the heading angle of the robot have variations on two time scales. However, the heading angle does not deviate from zero by more than $8°$ and periodically returns to zero. The path of the robot is shown in Fig. 6 with the heading angle indicated by the orientation of the longitudinal axis (shown by red lines) of
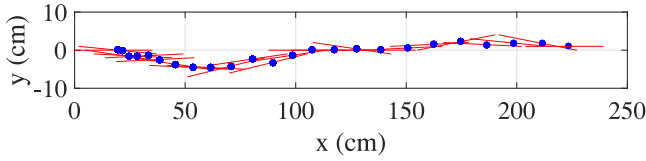
Fig. 6. Path of the robot for the case $\phi_r = \pi/3$ and $\omega_r = 2.98\pi$. The blue dots show the center of mass of the robot. The red lines show the longitudinal axis of the robot indicating its heading angle.

TABLE I
SURGE SPEEDS OF AQUATIC ROBOTS

Cited Reference	Body Length [cm]	Weight [g]	Surge Speed [BL/s]
[31]	30	–	1.1
[9]	15	60	1
[32]	52	–	0.96
[8]	11.7	70	0.94
[33]	78	–	0.92
[34]	70	–	0.64
[35]	33.7	–	0.51
[36]	66.1	–	0.5
This work	36.5	1094	0.49
[18]	50	4200	0.44
[37]	55	–	0.4
[4]	14.8	68	0.35
[38]	24.2	540	0.31
[39]	99	1640	0.25
[40]	24.3	–	0.23
[17]	180	52 000	0.22
[41]	120	12 700	0.21
[5]	20	290	0.11
[6]	30	–	0.1

The speeds are in BL/s.

the robot. The center of mass of the robot is shown by the blue dots. On the average, the robot swims along a straight line with nearly zero-lateral drift. A video of this motion of the robot is available as supplementary information.

The video camera located above the pool recorded the position of the robot at a frame rate of 30 f/s. We measured the time intervals necessary for the robot to move by 10 cm along the length of the pool. This was done by observing the frames in the recorded movie when the head of the robot crossed grid lines. The average translational velocity of the robot (in the X-direction) during each time interval was thus calculated. It should be noted that this average velocity u_x is lower than its surge velocity V_x. The average velocities for the nine combinations of inputs ϕ_r and ω_r are shown in Fig. 7(a)–(c).

The general trend observed in the data shown Fig. 7(a)–(c) is that the average velocity of the robot increases as the velocity of the internal rotor increases. Furthermore, the average velocity of the robot decreases as the amplitude of the oscillations of the internal rotor increases. However, in our experiments, we have found that if the amplitude of oscillations decreases significantly below $\frac{\pi}{4}$, then the average velocity of the robot decreases sharply with the robot almost oscillating in place.

The highest average velocity that the robot achieves is about 18 cm/s [see Fig. 7(c)] which is half a body length per second. The last few data points in most cases shown in Fig. 7 show
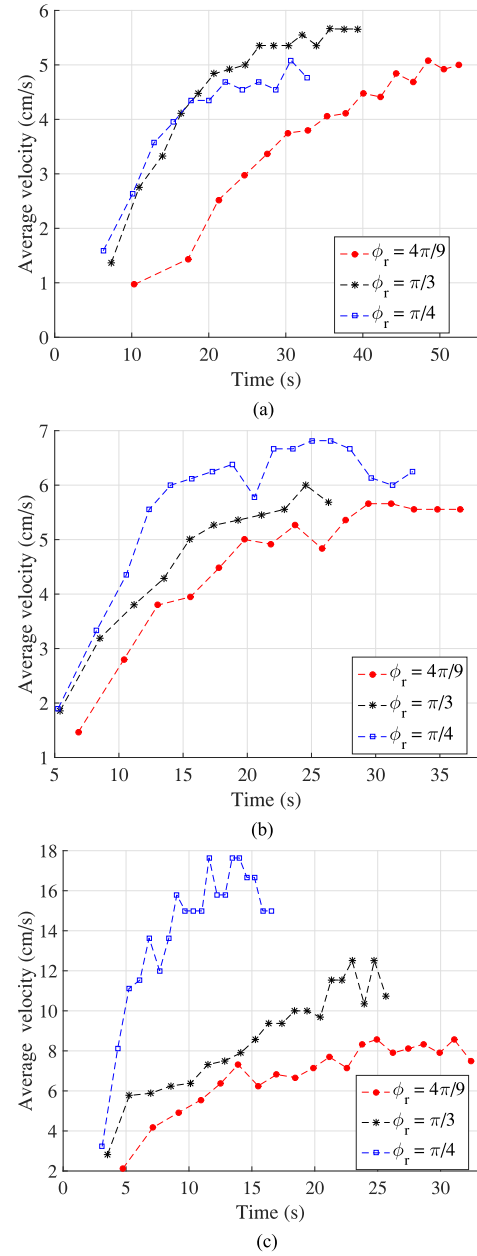

Fig. 7. Average velocity of the robot. (a) $\omega_r = 1.76\pi$ rad/s. (b) $\omega_r = 2.09\pi$ rad/s. (c) $\omega_r = 2.98\pi$ rad/s.

a decrease in the velocity of the robot, due to the fact that the robot approaches the walls of the pool.

We compared the average translational velocity in the best case to the velocities of other aquatic robots in Table I. The velocities we used for comparison are nondimensionalized in terms of body lengths per second (BL/s). In doing such a comparison, we restricted our attention to those robots which were capable of a speed of at least 0.1 BL/s.

B. Maneuverability

The motion of the robot is on average along a straight line if the angular velocity of the rotor is the same both when it rotates in the clockwise direction and when it rotates in the counter-
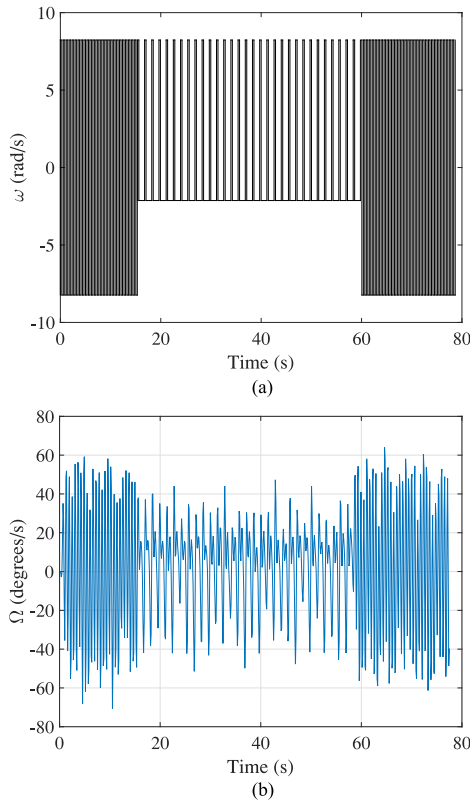
Fig. 8.   (a) Angular velocity of the ring and (b) angular velocity of the robot.

Fig. 9.   (a) Heading angle of the robot and (b) superimposed snapshots of the robot making a $180°$ turn.

clockwise direction. In case this is not so, the robot no longer moves along a straight line. We consider the case where the clockwise motion of the rotor is faster than its counter clockwise motion. A natural way to realize this with the servo motor is where the angular velocity is also piecewise constant, for example, as shown in Fig. 8(a). In the experiment to demonstrate the direction reversal, the rotor first executed symmetric oscillations to let the robot gain a translational velocity. The angular velocity of the rotor for this phase of motion is 8.23 rad/s, shown in the (symmetric) first part of Fig. 8(a). Then, the angular velocity of the rotor is asymmetric with the speed being 8.23 rad/s in the clockwise direction and 2.13 rad/s in the counter clockwise direction with the amplitude of the oscillations being $\frac{4}{9}\pi$. This is shown in the middle (asymmetric) part of the graph in Fig. 8(a). Once the robot makes a complete $180°$ turn, the rotor executes symmetric motion again. The angular velocity of the robot during this entire maneuver is shown in Fig. 8(b).

The direction reversal is further illustrated through the graph of the heading angle of the robot, Fig. 9(a). The robot which initially moves along a straight line on average makes a $180°$ turn and begins to move again along a straight line. The superimposed snapshots of the robot executing this maneuver are shown in Fig. 9(b). It took the robot 43 s to make the $180°$ turn. The turning radius for this motion was approximately 75 cm, i.e., about two body lengths. A video of the robot performing this maneuver is available as supplementary information.

The amount of time required and the turning radius were large compared to many biological swimmers. This is because of the
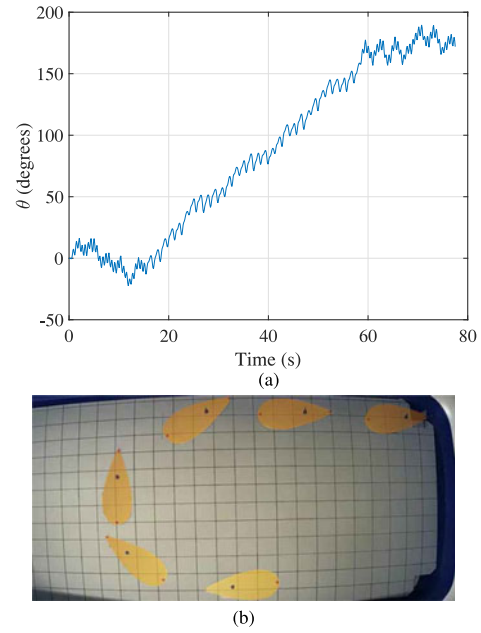
specific implementation of the concept of the internal rotor. Since a servo (without the capability of continuous rotation) was used to drive the rotor, both clockwise and counterclockwise rotations are necessary to execute almost any turn. Therefore, in each such asymmetric rotation of the rotor, the robot first turns in one direction and, then, back in the opposite direction, with the difference being the net angular displacement. This is illustrated by the heading angle in Fig. 9 which shows both increases and decreases but with the average angular displacement being an increasing function. An implementation of the robot with an internal rotor driven by DC motor could avoid this problem and allow the rotor to spin continuously in one direction at a high speed. The robot in such circumstances could potentially have the capability to execute a rapid maneuver with a small turning radius.

V. CONCLUSION AND FUTURE WORK

In this paper, we presented a proof-of-concept model of an underactuated planar swimming aquatic robot. The robot is propelled by means of an internal rotor and does not possess any external fins, propellers, or articulated joints. Its design and fabrication are therefore easy and the robot could have useful applications where stealth is required. The rotor is powered by a servo motor powered by batteries. The paper presents the details of the design of the robot and experimental data on its locomotion and maneuverability. It demonstrates that even with a preliminary design the robot is capable of achieving significant speeds.

The design of the robot is motivated by an idealized mathematical model of the interaction of a body with singular distributions of vorticity. The robot is capable of swimming due to an exchange of momentum between the body and the fluid that is mediated by vortex shedding. This mechanism of propulsion is

very similar to the way carangiform fish swim. Carangiform fish propulsion is made possible by the motion of a tail which causes the creation of vorticity. The physical shape variable is equivalent in a mathematical sense to the motion of the internal rotor.

There is further fundamental significance to the robot presented in this paper. The motion of the robot is controlled merely by controlling a single servo motor. The ease of actuation together with a qualitative mathematical model makes the robot a good testbed for several single-input motion and path control strategies, central pattern generators, and hydrodynamic interaction in a collection of robots.

In future work, several improvements and changes are planned that allow the robot to move in three dimensions as well as increase its propulsive efficiency and maneuverability. Three-dimensional swimming motion can be achieved through the use of a second rotor that spins along an axis perpendicular to the longitudinal axis of the robot. Alternatively, depth control of the robot could be buoyancy driven as in the case of an underwater glider. However, unlike a glider, the robot is not reliant on buoyancy for propulsion. The robots maneuverability can be improved via the addition of an unactuated flexible tail that can change the location where vorticity is shed. We also plan to integrate sensor data to implement feedback control of the motion of the robot.

References

[1] M. S. Triantafyllou and G. S. Triantafyllou, "Propulsion through oscillating foils in nature and technology," *J. Fluids Struct.*, vol. 7, pp. 205–224, 1993.

[2] M. S. Triantafyllou and G. Triantafyllou, "An efficient swimming machine," *Sci. Amer.*, vol. 272, no. 3, pp. 64–70, 1995.

[3] S. McGovern, G. Alici, Van-Tan Truong, and G. Spinks, "Finding nemo (novel electromaterial muscle oscillator): A polypyrrole powered robotic fish with real-time wireless speed and directional control," *Smart Mater. Struct.*, vol. 18, no. 9, 2009, Art. no. 095009.

[4] B. P. Epps, K. Youcef-Toumi, P. V. Alvarado, and A. H. Techet, "Swimming performance of a biomimetic compliant fish-like robot," *Experiments Fluids*, vol. 47, pp. 927–939, 2009.

[5] Z. Chen, S. Shatara, and X. Tan, "Modeling of biomimetic robotic fish propelled by an ionic polymermetal composite caudal fin," *IEEE/ASME Trans. Mechatronics*, vol. 15, no. 3, pp. 448–459, Jun. 2010.

[6] C. Rossi, J. Colorado, W. Coral, and A. Barrientos, "Bending continuous structures with SMAs: A novel robotic fish design," *Bioinspiration Biomimetics*, vol. 6, 2011, Art. no. 045005.

[7] M. Rufo and M. Smithers, "Ghostswimmer AUV: Applying biomimetics to underwater robotics for achievement of tactical relevance," *Marine Technol. Soc. J.*, vol. 45, no. 4, pp. 24–30, 2011.

[8] V. Kopman and M. Porfiri, "Design, modeling, and characterization of a miniature robotic fish for research and education in biomimetics and bioinspiration," *IEEE/ASME Trans. Mechatronics*, vol. 18, no. 2, pp. 471–483, Apr. 2013.

[9] V. Kopman, J. Laut, A. R. Acquaviva, and M. Porfiri, "Dynamic modeling of a robotic fish propelled by a compliant tail," *IEEE J. Ocean. Eng.*, vol. 40, no. 1, pp. 209–221, Jan. 2015.

[10] K. A. Morgansen, B. I. Triplett, and D. J. Klein, "Geometric methods for modeling and control of free-swimming fin-actuated underwater vehicles," *IEEE Trans. Robot.*, vol. 23, no. 6, pp. 1184–1199, Dec. 2007.

[11] L. H. Long Jr., N. M. Krenitsky, S. F. Roberts, J. Cirokawa, J. de Leeuw, and M. E. Porter, "Testing biomimetic structures in bioinspired robots: How vertebrae control the stiffness of the body and the behavior of fish-like swimmers," *Integrative Comput. Biol.*, vol. 51, no. 1, pp. 158–175, 2011.

[12] H. Xiong, "Geometric mechanics, ideal hydrodynamics, and the locomotion of planar shape-changing aquatic vehicles," Ph.D. dissertation, Univ. of Illinois at Urbana-Champaign, Champaign, IL, USA, 2007.

[13] B. Allotta et al., "The arrows project: Adapting and developing robotics technologies for underwater archaeology," *IFAC-Papers Online*, vol. 48, no. 2, pp. 194–199, 2015.

[14] C. C. Eriksen et al., "A longrange autonomous underwater vehicle for oceanographic research," *IEEE J. Ocean. Eng.*, vol. 26, no. 4, pp. 424–436, Oct. 2001.

[15] J. Sherman, R. E. Davis, W. B. Owens, and J. Valdes, "The autonomous underwater glider 'spray'," *IEEE J. Ocean. Eng.*, vol. 26, no. 4, pp. 437–446, Oct. 2001.

[16] D. C. Webb, P. J. Simonetti, and C. P. Jones, "Slocum: An underwater glider propelled by environmental energy," *IEEE J. Ocean. Eng.*, vol. 26, no. 4, pp. 447–452, Oct. 2001.

[17] D. L. Rudnick, R. E. Davis, C. C. Eriksen, D. M. Fratantoni, and M. J. Perry, "Underwater gliders for ocean research," *Marine Technol. Soc. J.*, vol. 38, no. 2, pp. 73–84, 2004.

[18] F. Zhang, T. John, C. Thon, and X. Tan, "Miniature underwater glider: Design and experimental results," *IEEE/ASME Trans. Mechatronics*, vol. 19, no. 1, pp. 394–399, Feb. 2014.

[19] P. Tallapragada, "A swimming robot with an internal rotor as a nonholonomic system," in *Proc. Amer. Control Conf.*, 2015, pp. 657–662.

[20] P. Tallapragada and S. D. Kelly, "Up a creek without a paddle: Idealized aquatic locomotion via forward vortex shedding," in *Proc. 5th ASME Dyn. Syst. Control Conf.*, 2012, pp. 221–225.

[21] P. Tallapragada and S. D. Kelly, "Reduced-order modeling of propulsive vortex shedding from a free pitching hydrofoil with an internal rotor," in *Proc. 2013 Amer. Control Conf.*, 2013, pp. 615–620.

[22] P. Tallapragada and S. D. Kelly, "Self-propulsion of free solid bodies with internal rotors via localized singular vortex shedding in planar ideal fluids," *Eur. Phys. J. Special Topics*, vol. 224, no. 17, pp. 3185–3197, 2015.

[23] K. Streitlien and M. S. Triantafyllou, "Force and moment on a Joukowski profile in the presence of point vortices," *AIAA J.*, vol. 33, no. 4, pp. 603–610, 1995.

[24] B. N. Shashikanth, J. E. Marsden, J. W. Burdick, and S. D. Kelly, "The Hamiltonian structure of a 2d rigid circular cylinder interacting dynamically with n point vortices," *Phys. Fluids*, vol. 14, no. 3, pp. 1214–1227, 2002.

[25] E. Kanso, "Swimming in an inviscid fluid," *Theor. Comput. Fluid Dyn.*, vol. 24, pp. 201–207, 2010.

[26] S. D. Kelly and H. Xiong, "Self-propulsion of a free hydrofoil with localized discrete vortex shedding: Analytical modeling and simulation," *Theor. Comput. Fluid Dyn.*, vol. 24, no. 1, pp. 45–50, 2010.

[27] Sir H. Lamb, *Hydrodynamics*. New York, NY, USA: Dover, 1945.

[28] E. Kanso, J. E. Marsden, C. W. Rowley, and J. B. Melli-Huber, "Locomotion of articulated bodies in a perfect fluid," *J. Nonlinear Sci.*, vol. 15, pp. 255–289, 2005.

[29] T. Chambrion and A. Munnier, "Locomotion and control of a self-propelled shape-changing body in a fluid," *J. Nonlinear Sci.*, vol. 21, pp. 325–385, 2011.

[30] L. M. Milne-Thomson, *Theoretical Hydrodynamics*. New York, NY, USA: Dover, 1996.

[31] P. Valdivia y Alvarado and K. Youcef-Toumi, "Design of machines with compliant bodies for biomimetic locomotion in liquid environments," *ASME J. Dyn. Syst. Meas. Control*, vol. 128, pp. 3–13, 2006.

[32] J. D. Liu and H. Hu, "Biologically inspired behaviour design for autonomous robotic fish," *Int. J. Autom. Comput.*, vol. 3, no. 4, pp. 336–347, 2006.

[33] D. Shin, S. Y. Na, J. Y. Kim, and S. J. Baek, "Fuzzy neural networks for obstacle pattern recognition and collision avoidance of fish robots," *Soft Comput.*, vol. 12, no. 7, pp. 715–720, 2007.

[34] W. Wang, J. Yu, R. Ding, and M. Tan, "Bio-inspired design and realization of a novel multimode amphibious robot," in *Proc. IEEE Int. Conf. Autom. Logistics*, Shenyang, China, 2009, pp. 140–145.

[35] E. Papadopoulos, E. Apostolopoulos, and P. Tsigkourakos, "Design, control, and experimental performance of a teleoperated robotic fish," in *Proc. 17th Mediterranean Conf. Control Autom.*, 2009, pp. 766–771.

[36] K. H. Low, "Current and future trends of biologically inspired underwater vehicles," in *Proc. IEEE Defense Sci. Res. Conf. Expo.*, 2011, pp. 1–8.

[37] R. Fan, J. Yu, L. Wang, G. Xie, Y. Fang, and Y. Hu, "Optimized design and implementation of biomimetic robotic dolphin," in *Proc. IEEE Int. Conf. Robot. Biomimetics*, 2005, pp. 484–489.

[38] L. Cen and A. Erturk, "Bio-inspired aquatic robotics by untethered piezo-hydroelastic actuation," *Bioinspiration Biomimetics*, vol. 8, 2013, Art. no. 016006.

[39] L. Manfredi *et al.*, "A bioinspired autonomous swimming robot as a tool for studying goal-directed locomotion," *Biol. Cybern.*, vol. 107, no. 5, pp. 513–527, 2013.

[40] Z. Wang, Y. Wang, J. Li, and G. Hang, "A micro biomimetic manta ray robot fish actuated by SMA," in *Proc. 2009 IEEE Int. Conf. Robot. Biomimetics*, 2009, pp. 1809–1813.

[41] F. Liu, K. M. Lee, and C. J. Yang, "Hydrodynamics of an undulating fin for a wave-like locomotion system design," *IEEE/ASME Trans. Mechatronics*, vol. 17, no. 3, pp. 554–562, Jun. 2012.

Phanindra Tallapragada received the B.Tech. and M.Tech. degrees from the Indian Institute of Technology, Kharagpur, India, in 2004. He received the M.S. degree in mathematics and Ph.D. degree in engineering mechanics from Virginia Polytechnic and State University, Blacksburg, VA, USA, in 2010.

He was a Postdoctoral Fellow in the Department of Mechanical Engineering and Engineering Science, University of North Carolina, Charlotte, NC, USA, between 2010 and 2013. He has been an Assistant Professor in the Department of Mechanical Engineering, Clemson University, Clemson, SC, USA, since August 2013.

His current research interests include dynamical systems, geometric mechanics, nonholonomic mechanical systems, vortex dynamics, bio-inspired swimming robots, and locomotion in low Reynolds number flows.

Beau Pollard received the B.S. degree in mechanical engineering from Clemson University, Clemson, SC, USA, in 2015, where he is currently working toward the Ph.D. degree in mechanical engineering in the Department of Mechanical Engineering.

His current research interests include nonlinear dynamics, bio inspired swimming robots, and low-dimensional models of fluid-structure interaction.